LAWRENCE
LIVERMORE
NATIONAL
LABORATORY

LLNL-PROC-493139

Interferometric Adaptive Optics Testbed for Laser Pointing, Wave-Front Control and Phasing

K. L. Baker, D. C. Homoelle, E. Utterback, E. A. Stappaerts, C. W. Siders, C. P. J. Barty

December 15, 2009

SPIE Photonics West Micro-Opto-Electro-Mechanical Systems-Microelectromechanical Systems 2010
San Francisco, California
January 25-27, 2010

This document was prepared as an account of work sponsored by an agency of the United States government. Neither the United States government nor Lawrence Livermore National Security, LLC, nor any of their employees makes any warranty, expressed or implied, or assumes any legal liability or responsibility for the accuracy, completeness, or usefulness of any information, apparatus, product, or process disclosed, or represents that its use would not infringe privately owned rights. Reference herein to any specific commercial product, process, or service by trade name, trademark, manufacturer, or otherwise does not necessarily constitute or imply its endorsement, recommendation, or favoring by the United States government or Lawrence Livermore National Security, LLC. The views and opinions of authors expressed herein do not necessarily state or reflect those of the United States government or Lawrence Livermore National Security, LLC, and shall not be used for advertising or product endorsement purposes.

This work performed under the auspices of the U.S. Department of Energy by Lawrence Livermore National Laboratory under Contract DE-AC52-07NA27344.

Interferometric adaptive optics testbed for laser pointing, wave-front control and phasing

K.L. Baker*[a], D.C. Homoelle[a], E. Utterback[a], E.A. Stappaerts[b], C.W. Siders[a], C.P.J. Barty[a]
[a]Lawrence Livermore National Laboratory, 7000 East Ave., Livermore, CA, USA 94550-0345
[b]Stappaerts Consulting, LLC, San Ramon, CA

ABSTRACT

Implementing the capability to perform fast ignition experiments, as well as, radiography experiments on the National Ignition Facility (NIF) places stringent requirements on the control of each of the beam's pointing, intra-beam phasing and overall wave-front quality. In this article experimental results are presented which were taken on an interferometric adaptive optics testbed that was designed and built to test the capabilities of such a system to control phasing, pointing and higher order beam aberrations. These measurements included quantification of the reduction in Strehl ratio incurred when using the MEMS device to correct for pointing errors in the system. The interferometric adaptive optics system achieved a Strehl ratio of 0.76 when correcting for a piston, tip/tilt error between two adjacent rectangular apertures, the geometry expected for the National ignition Facility. The interferometric adaptive optics system also achieved a Strehl ratio of 0.66 when used to correct for a phase plate aberration of similar magnitude as expected from simulations of the ARC beam line. All of these corrections included measuring both the upstream and downstream aberrations in the testbed and applying the sum of these two measurements in open-loop to the MEMS deformable mirror.
Keywords: Adaptive Optics, Short-Pulse Lasers, Wave-front sensing, Interferometry

*baker7@llnl.gov; phone 1 925 422-1461; fax 1 925 422-1796

1. INTRODUCTION

Numerous laser systems currently employ, or have employed in the past, adaptive optics (AO) systems to correct their wave-front aberrations. These aberrations can be caused by many mechanisms which include thermal distortions in the amplifiers, temperature fluctuations, stress-induced birefringence, damage spots on and inherent aberrations in the optical components, nonlinear effects, vibrations and misalignment of optics. The laser systems with AO include the largest lasers currently being built, the National Ignition Facility[1] and the Laser Megajoule, the NOVA petawatt laser[2], the beamlet laser[3], the LULI laser system[4], the Vulcan petawatt laser[5], to name a few. These lasers have exclusively used conventional Shack-Hartmann and shear-interferometer systems which measure the gradient in the wave-front and as such are unable to measure the piston error between multiple beams.

The National Ignition Facility (NIF) will become fully operational this calendar year and incorporates 192 400 mm aperture Nd:glass beam lines. A schematic of one of the beam lines of NIF is shown in Fig. 1. One quad of the 192 NIF beams is designated for x-ray backlighting and fast ignition experiments. Each of these four square NIF Beams is split into two rectangular beam lines. As such eight rectangular beams that can be independently pointed are formed from the original four square NIF beams. Each of these eight beams focuses to the target chamber center as an f/22 by f/44 beam. These beam lines will differ from the standard NIF beam line in several ways. A fiber-based short pulse will be added to the master oscillator to seed a quad of main amplifiers. The short pulse is stretched in pulse length before entering the preamplifer modules and then compressed to a 1-10 ps pulse with a vacuum compressor placed on the target area mezzanine. The eight 1.053 μm short pulse laser beams will then be focused near target chamber center with an off-axis parabola to minimize B integral effects. Each of these eight beams will deliver a laser pulse to chamber center that is nominally 5 ps in pulse length and 995 J in energy, giving an overall energy of 7.96 kJ delivered to the target. The fast ignition experiments require that 4 kJ of the total 7.96 kJ of laser energy be deposited within a 40 μm diameter circle. Each of the eight beams focuses to the target chamber center as an f/22 by f/44 beam such that the first lobe of the diffraction pattern represents a rectangular shape of ~ 46 by 93 μm in the far-field. At the very least each of the two beams formed from a single NIF beam must be phased together to meet the enclosed energy requirement. The approximate pupil geometry of the eight beams is shown below in Fig 2a along with the far-field pattern, in Fig. 2b,

generated by this pupil assuming that all of the beams are in phase and no phase aberrations are present. Fig. 2b also contains a 40 μm diameter circle showing the spatial dimensions of the focused beams. If all the beams are phased and pointed together and fully corrected with a Strehl ratio, S_r, of 1, then they would deliver 5.6 kJ in a 40 μm diameter circle, exceeding the requirements by 1.6 kJ. When each of the two beams formed from a single NIF beam are co-phased, but with random piston errors between the four beam pairs, the encircled energy requirement of 4 kJ is exceeded 90% of the time provided the Strehl ratio is greater than 0.72.[6] This latter statement was determined by analyzing the results from a thousand simulations to evaluate the system performance with random piston errors, random tip/tilt errors and a random realization of a residual turbulence profile applied to the eight beams. The random realization of the residual turbulence profile consisted of a Von Karman turbulence profile with the Fried parameter r_o=D/8 and the outer scale length set to D/2 with D representing the longest aperture dimension. In the case of tip/tilt errors, normally-distributed pseudo-random numbers with a mean of zero and a standard deviation of 1 μrad were assigned to both the tip and tilt components of the phase. The Von Karman turbulence parameters were chosen based upon residual wave-front measurements taken on one of the NIF beam lines after a low order deformable mirror was utilized to pre-correct for wave-front aberrations in the rod and disk amplifiers caused primarily by heat deposition from the flashlamps.[6] A Von Karman turbulence profile is also expected from the gas turbulence inside the beam tubes due the natural truncation of the outer scalelength of the turbulence spectrum by the beam tubes enclosing the optics.

An interferometric wave-front sensor was chosen for the task of correcting these beam lines in part due to the fact that these systems measure the phase directly and as such can determine the piston difference between apertures. The ability to measure piston errors is one such advantage of an interferometric adaptive optics system over conventional adaptive optics systems such as Shack-Hartmann and curvature sensors which measure the first and second derivative of the phase, respectively.[7] Interferometric adaptive optics systems have been proposed and implemented previously to correct for atmospheric aberrations[8,9] and to function as extreme adaptive optics systems.[10,11] A testbed was constructed to experimentally evaluate the ability of the interferometric wavefront sensor to correct the types of aberrations expected on the ARC beam lines as described in section 2. The types of aberrations expected on the ARC beam line were evaluated experimentally on the testbed as detailed in section 3 and these aberrations consisted of tip/tilt control of the beamlines, piston and tip/tilt errors between adjacent rectangular apertures and Von Karman turbulence profiles of the levels expected on the ARC beam lines. The measured Strehl ratios are compared with analytical expectations in section 4 and discrepancies between the measured and theoretical Strehl ratios due to hardware limitations are discussed in the fifth section.

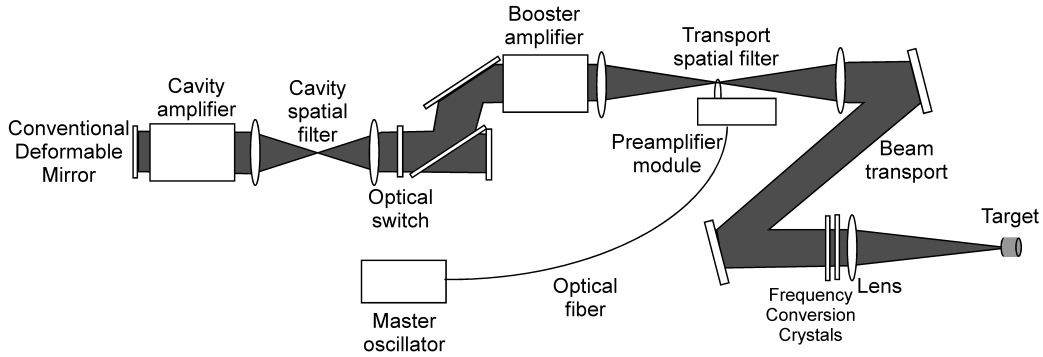

Fig. 1. Schematic of the major components of a National Ignition Facility (NIF) laser beam from injection to final focus.

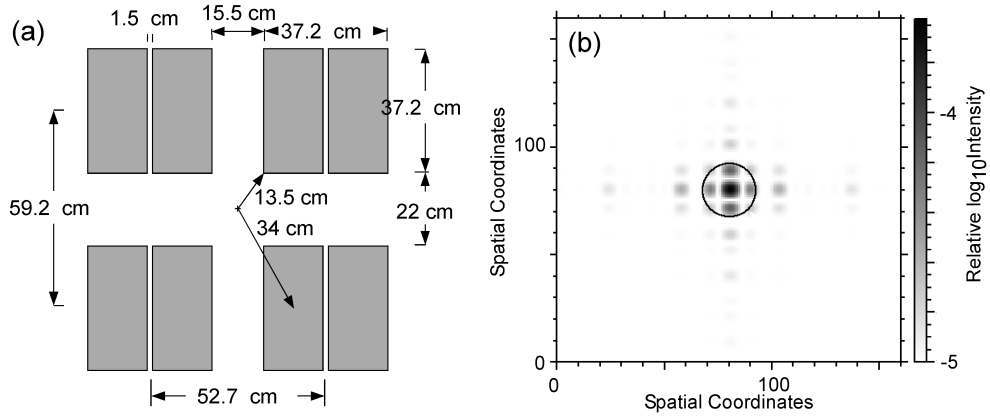

Fig. 2. Pupil layout for the advanced radiography capability on the National Ignition Facility is displayed in Fig.2a. The pupil represents four beam pairs with each of the beam pairs containing 1.99 kJ centered around 1.053 μm in a 5 ps pulse. Fig. 2b shows the far-field pattern generated from this pupil assuming that all of the beams are pistoned correctly and have a perfect Strehl ratio.

2. TESTBED LAYOUT

A testbed was designed and built to examine the capabilities of the interferometric adaptive optics system to successfully correct the aberrations expected on the ARC diagnostic. The optical layout of the IR laboratory breadboard system is shown in Fig. 3. It consists of five main components; an interferometric wave-front sensor, a MEMS-based spatial-light-modulator built by the Boston Micromachines Corporation (BMC), two tip/tilt mirrors, a 1053 nm Nd:YLF laser and computer hardware/software to analyze the wave-front and implement the phase correction. The deformable mirror can be run in either open or closed-loop operation but has thus far been run exclusively in open loop. The Nd:YLF laser is split into three separate beams using polarizing beamsplitters and has a nearly transform-limited pulse of 2 ns duration and a pulse energy of 35 μJ. The testbed is designed to evaluate the performance of both segmented and continuous phase sheet MEMS devices, however, a segmented MEMS has been used thus far. The segmented devices do not require a wave-front reconstruction, however, the continuous face sheet MEMS devices will require a phase-unwrapping wave-front reconstruction to be performed in order to avoid 2π phase jumps being applied to the continuous surface.

Polarization components are utilized in the testbed to form the two interferograms with a π/2 phase shift between the reference beams in these interferograms. The probe beam passes through a square aperture that is relay imaged onto the MEMS-based spatial light modulator in open-loop operation. The MEMS device is then relay imaged onto the partial reflector, APR, which is relay imaged onto the focal plane array. At the APR, in the upper right of Fig. 3, a percentage of the probe beam is reflected and travels back upstream to a beam splitter which sends part of the probe into the interferometric wave-front sensor, upper left of Fig. 3. The probe beam passes through a half wave plate that rotates its polarization by π/4, producing equal amplitude horizontal and vertical components of the probe beam before it is combined with the reference beam. The reference beam passes through a thin film polarizer near the top of Fig. 3 and the resulting p-polarized beam passes through a quarter wave plate (QWP) at 45 degrees to vertical, which converts the linearly polarized light into circularly polarized light with a π/2 phase shift between orthogonal polarizations. After the reference beam passes through the QWP, the reference and probe beams, in either the open or closed loop geometries, are combined using a non-polarizing 50/50 beamsplitter, in the center near the top of Fig. 3. The reference and probe beams then pass through a telescope shown in the upper left-hand side of Fig. 3. A Wollaston prism, at the focus of the first telescope lens, separates the two interferograms in angle. The two interferograms, having orthogonal polarizations, exit the Wollaston prism at an angle of approximately 1.93 degrees with respect to one another and are collimated by the two lenses placed directly after the Wollaston prism. The two spatially separated interferograms are then directed to the IR camera, which is in a conjugate plane to the spatial light modulator and to the entrance aperture of the system. Part of the probe beam passes through the APR and is relay imaged to the position of the MEMS device in closed-loop located near the center of Fig. 3. This plane is then relay imaged onto two subsequent tip/tilt mirrors, one used to simulate vibrations and the other to correct the simulated vibrations. The last tip/tilt mirror is then relay imaged to a plane where phase plates add turbulence onto the beam in the lower left-had side of Fig. 3. This is the location where the phase plate was situated for the measurements discussed below. This plane is relay imaged onto the focusing optic, a 1 m f.l. lens,

which then focuses the probe beam onto the backlighter fiber shown in the bottom left-hand corner of Fig. 3. Tracking cameras are used to measure the Strehl ratio and the tip/tilt correction of the system and an additional tracking camera is placed in the interferometric wave-front sensor arm near the Wollaston prism to evaluate offloading of the tip/tilt correction with a CCD camera by tracking the spot motion.

The two interferogams provide the sine and cosine channels, however, there are three unknowns and additional information is required to unwrap the phase. The three unknowns are the reference beam electric field, the probe beam electric field and the phase. To provide additional information, the reference aperture is oversized relative to the probe beam. By measuring the spatial profile of the reference beam before the correction run and using the oversized region on the detector to scale the measured reference amplitude on each measurement, the detector effectively provides a measurement of the reference beam intensity on each shot as well. By setting the probe beam intensity much lower than the reference beam and neglecting this component in the interferograms, the phase can be uniquely determined.

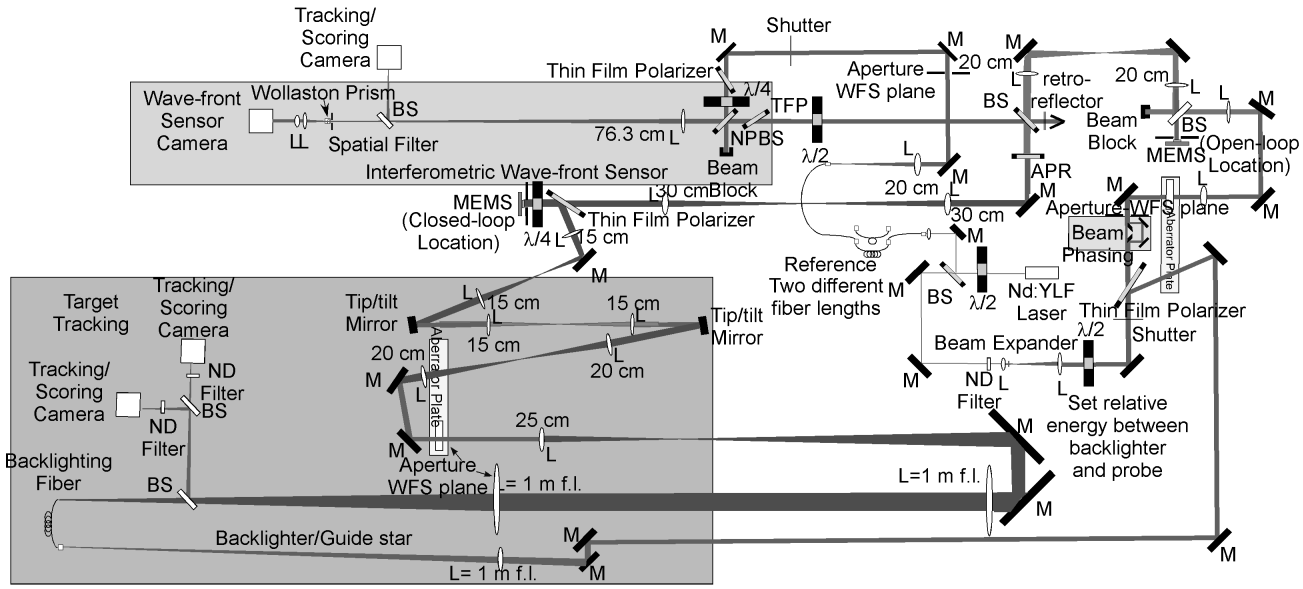

Fig. 3. Laboratory breadboard setup used to test the performance of the phase conjugate engine in a controlled laboratory environment. The abbreviations stand for the following: BS, beam splitters; M, mirrors; L, lenses; S, shutters; A, apertures; TFP, thin film polarizers; λ/2 and λ /4, half and quarter wave-plates, respectively. The dimensions primarily refer to the focal length of the lenses and mirrors.

The interferometric system would be implemented on the National Ignition Facility as shown in Fig. 4. The guide star for the adaptive optics system, in the case of x-ray backlighting, would come from optical fibers embedded in the backlighter target, which would consist of up to eight high atomic number (high Z) wires embedded in a low atomic number (low Z) material. The low Z material is used to tamp the expansion of the high Z material so that the backlighting x-rays produced in the laser-plasma interaction emanate from a small spatial extent. Fibers are placed next to the high Z wires to guide each of the eight ARC beams to their respective high Z wire. The laser backlighter is sent through each of the eight fibers and each of the eight beamlets then propagate back through their respective laser chain after being collimated by the off-axis parabola. A rotating quarter wave-plate chopper is used in the cavity spatial filter to allow the signal to back propagate through the cavity amplifier at hundreds to thousands of hertz. The plasma electrode pockel cell (PEPC) that resides in the cavity spatial filter only allows signals to pass through at 0.2 hz without this rotating wave-plate chopper, which would be insufficient to correct vibrational movement of the optical train. The signals would then back propagate to the preamplifier module where the interferometric wave-front sensor, tip/tilt mirror and deformable mirror would measure and correct the tip/tilt and higher order aberrations in the optical train, respectively. This correction would happen in the same manner as on the testbed shown in Fig. 3 and discussed in this

article. The wave-front sensor would measure the aberrations in the optical train upstream of the sensor using the reflection from the partial reflector, APR, to interfere with the reference beam. The retro-reflector, RR, would be used to initially set the reference beam such that the optical axis of the laser coincided with that of the reference beam. The retro-reflector would then be blocked for the upstream measurement of the laser. The wave-front sensor would measure the downstream aberrations in the laser using the interference between the reference beam and fiber backlighters originating near the target chamber center. The path length of the reference laser must be changed between these measurements to allow the reference beam to interfere with the upstream and downstream probe pulses. The upstream and downstream aberrations would then be added together and applied to the deformable mirror along with open loop corrections.[6,12] The open loop corrections include expected changes between the last measurement of the AO system and when the laser pulse is fired, as well as, accounting for the pointing offset and distance between the fiber backlighter and the desired focal spot at the end of the fast ignition cone in the case of fast ignition experiments. The latter open-loop correction involves placing a slight tip/tilt and focus term on each of the beams to steer them to the correct location before the laser shot. The tip/tilt system would run in closed-loop removing the pointing errors of the optical train components.

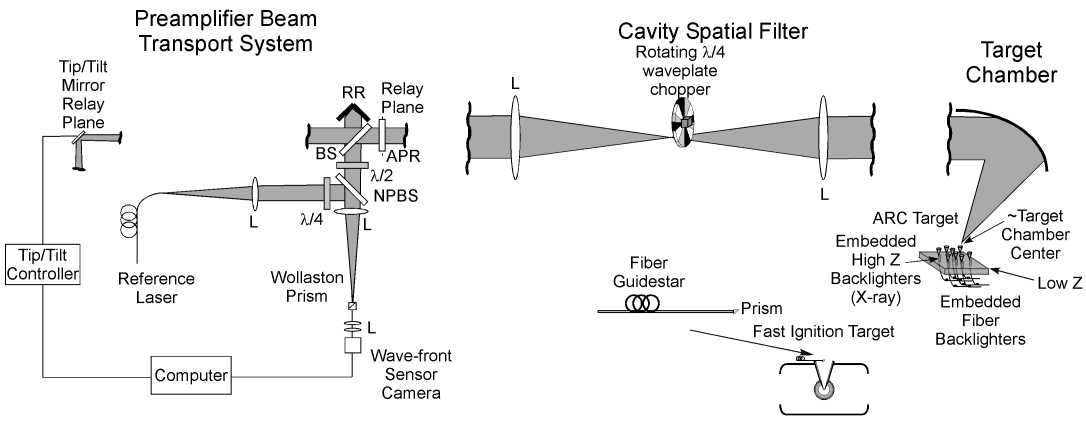

Fig. 4. Implementation of the interferometric adaptive optics system on the National Ignition Facility. The abbreviations stand for the following: BS, beam splitters; L, lenses; λ/2 and λ /4, half and quarter wave-plates, respectively.

3. MEASUREMENTS ON THE TESTBED

The final stage of correction for the fast ignition capability on the ARC diagnostic involves placing a slight tip/tilt and focus term on each of the beams to steer the beams off of the fiber backlighter and correct the ~ 5x10-4 change in the focal length. The change in tip/tilt between the individual beams focusing on the targeting sphere and the end of the fast ignition cone is slight, $\alpha(\Delta x/f.l.)$, where α is the angle of the guide star beam from the optical axis of the ARC pupil, f.l. is the focal length of the parabola and Δx is the distance between the fiber backlighter and the end of the fast ignition cone. For each of the beam pairs forming the ARC pupil this corresponds to an applied tilt of 18.8 μrad or a peak-to-valley phase tip/tilt of 6.9 μm. The difference in the focal length imposed on the MEMS devices to make the required changes to the focus of the parabola is a peak-to-valley defocus of 0.66 μm. The application of the tip/tilt phase on the MEMS device causes a slight reduction in the Strehl ratio and this reduction was studied on the testbed, as well as, analytically.

In the "spirit" of adaptive optics, the Strehl ratio can be calculated from the phase variance, σ^2, using the Marechal approximation, $S_r \sim \exp(-\sigma^2)$.[13] For a given number of bits, n, the number of phase correction levels is given by 2^n. Each level of correction covers a phase region of $\phi_o = 2\pi/2^n$ radians. The phase variance within each of the correction levels is given by

$$\sigma^2 = \frac{1}{m}\sum_{i=0}^{m-1}\left(\phi_i - \phi_{avg}\right)^2 , \qquad (1$$

where m represents the number of phase levels and ϕ_{avg} is the central phase within a particular correction level. Assuming a uniform distribution of phases, Eq. 1 can be approximated by

$$\sigma^2 \approx \frac{1}{\phi_o}\int_0^{\phi_o}\left(\phi-\phi_o/2\right)^2 d\phi = \left(\frac{\pi^2}{3}\right)\frac{1}{2^{2n}}. \quad (2$$

Using the "extended Marechal approximation", the Strehl ratio, S_r, can be expressed as $S_r \sim \exp\{-(\pi^2/3)/2^{2n}\}$. A more formal derivation, yields the expression $S_r = \mathrm{sinc}^2(\pi/2^n)$.[14] For a linear phase profile, tip or tilt, applied across all 32 MEMS rows, the number of correction bits, 2n, is equal to the number of waves of tilt across the MEMS device, Amp, divided by the number of actuator rows, 32. The Strehl ratio can then be expressed as $S_r \sim \exp\{-(\pi^2/3)(\mathrm{Amp}/32)^2\}$.

The loss of Strehl ratio due to the application of tilt across the MEMS device was tested on the system by applying increasingly larger levels of tilt to the MEMS device and measuring the far-field patterns. The far-field patterns for four different levels of tip applied to the MEMS device are shown in Fig. 5a. For this measurement a small aperture, ~ 2 mm square, was placed in front of the MEMS device such that aberrations from both the MEMS device itself and the optics in the testbed would be minimized. This enabled high Strehl ratios, S_r ~0.95, to be achieved with no tilt applied to the MEMS deformable mirror. In Fig 5a the number of waves of tilt applied to the MEMS deformable mirror from left to right was 0, 4, 8 and 12 waves, respectively. As the tilt applied to MEMS deformable mirror increases, it becomes a phase grating putting energy into multiple orders as seen in Fig. 5a. As the number of waves of tilt applied to the MEMS deformable mirror reaches 16, the MEMS device becomes a phase grating with a 180 degree phase shift between adjacent rows of pixels and an efficiency in the +1 order is ~43%. Fig. 5b illustrates the Strehl ratio as a function of the waves of tilt applied across the MEMS device. The squares represent the derived Strehl ratios from the measured far-field patterns shown in Fig. 5a. The solid black line represents the theoretical curve derived above and the solid grey curve is simply a vertical displacement of the analytical curve to account for the small level of aberrations present on the MEMS device and on the optical train of the testbed. The Strehl ratio was determined by comparing the peak of the measured far-field intensity distribution to simulated far-field patterns chosen to match the lobe pattern of the measured far-field distribution. For the expected amplitude of 6.9 microns of applied tilt required to move the beam from the fiber backlighter to the back of the fast ignition cone, the Strehl ratio would be degraded by ~0.13 which is a significant fraction of the error budget and so will be delegated to a separate tip/tilt mirror. The results of this study will be presented in an auxiliary paper.[15]

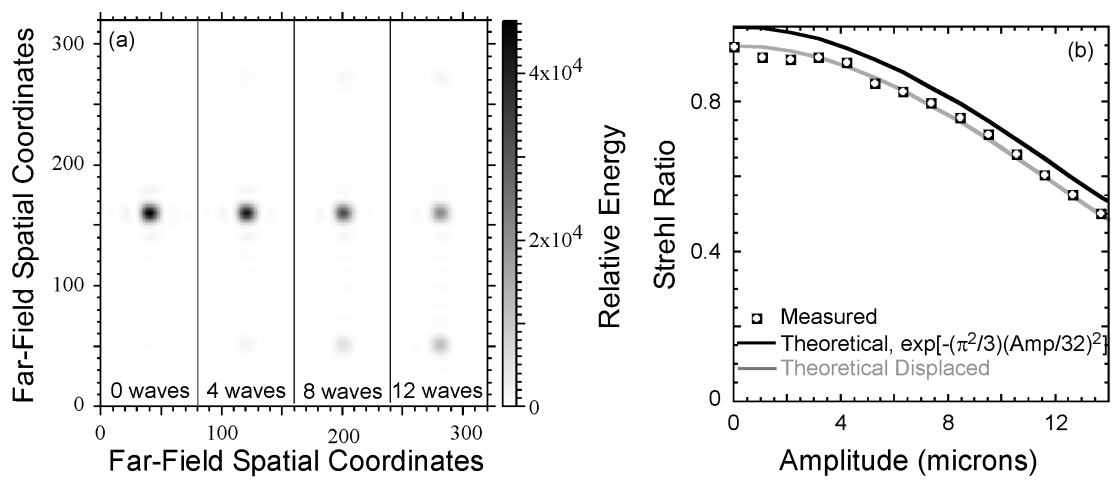

Fig. 5. Measurements examining the effects of applying tip/tilt to the MEMS device Fig. 3a represents the far-field intensity patterns at four separate values of tilt applied to the MEMS deformable mirror. Fig. 5b displays the Strehl ratio as a function of tilt amplitude applied to the MEMS deformable mirror. The squares represent the Strehl ratios derived from the measured far-field intensity patterns, the solid black line represents the theoretical Strehl ratio as a function of tilt and the solid grey line represents a vertical displacement of the solid black line.

A microscope slide was used to test the performance of the interferometric AO system to piston and tip/tilt differences between two apertures, represented as the upper and lower half of the MEMS device. The microscope slide was placed upstream of the wave-front sensor across half of the aperture. Initially the wrapped phase downstream of the

wave-front sensor, including the aberrations present in the testbed optics, was measured. The wrapped phase upstream of the wave-front sensor, including both the microscope slide and the MEMS deformable mirror, was then measured by changing the fiber length in the reference beam line such that it would interfere with the light from the laser. The upstream and downstream phases were then summed, the inverse taken and then wrapped and next applied to the MEMS deformable mirror. The results from the measurement and correction of the phase plate are shown in Fig. 6. The unwrapped phase from the microscope slide and the MEMS deformable mirror measurement are shown in Fig. 6a where the microscope slide was placed across the lower half of the MEMS device. The wrapped phase was unwrapped using the path following algorithm developed by Goldstein.[16,17,18] The microscope slide introduced both a piston phase difference between the upper and lower halves of the MEMS device, as well as a tip component of approximately 1 wave. The far-field intensity pattern with the phase correction applied to the MEMS device is displayed in Fig. 6b. The far-field intensity pattern was analyzed to determine the Strehl ratio by comparing the measured intensity pattern to simulated intensity patterns using Fourier transforms of a square aperture. The Strehl ratio of the corrected far-field pattern was determined to be S_r =0.76.

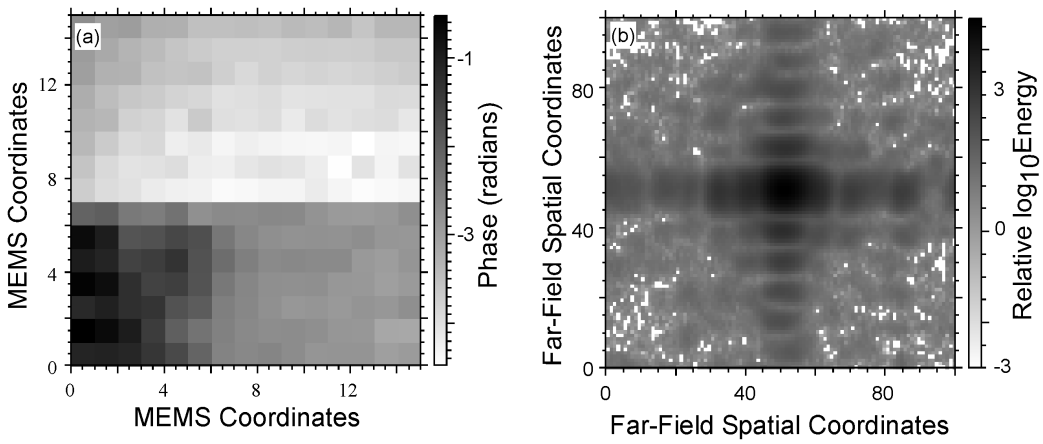

Fig. 6. Measurements examining the effects of piston errors between two adjacent rectangular apertures. The piston error was introduced by placing a microscope slide across the lower half of the MEMS device. The microscope slide introduced both a piston and tilt across one half of the MEMS device. Fig. 6a represents the unwrapped phase measured with the microscope slide across the lower half of the MEMS. Fig. 6b represents the far-field intensity pattern after the inverse phase was applied to the MEMS device.

A phase plate was used to test the performance of the interferometric AO system to a Kolmogorov turbulence profile. The phase plate was placed downstream of the wave-front sensor. Initially the wrapped phase upstream of the wave-front sensor, including the MEMS device, was measured. The wrapped phase downstream of the wave-front sensor was then measured by changing the fiber length in the reference beam line such that it would interfere with the light from the fiber backlighter. The upstream and downstream phases were then summed, the inverse taken and then wrapped and next applied to the MEMS deformable mirror. The results from the measurement and correction of the phase plate are shown in Fig. 7. The wrapped and unwrapped phases from the phase plate measurement are displayed in Fig. 7a and 7b, respectively. The wrapped phase was unwrapped using the path following algorithm developed by Goldstein.[16,17,18] The far-field intensity patterns without and with the phase correction applied to the MEMS device are displayed in Fig. 7c and 7d, respectively. Both of the far-field intensity patterns were analysed to determine the Strehl ratio by comparing the measured intensity pattern to simulated intensity patterns using Fourier transforms of a square aperture. The tip/tilt removed Strehl ratio of the uncorrected far-field pattern in Fig. 7c was determined to be S_r =0.087, while the Strehl ratio of the corrected far-field pattern was found to be S_r =0.66.

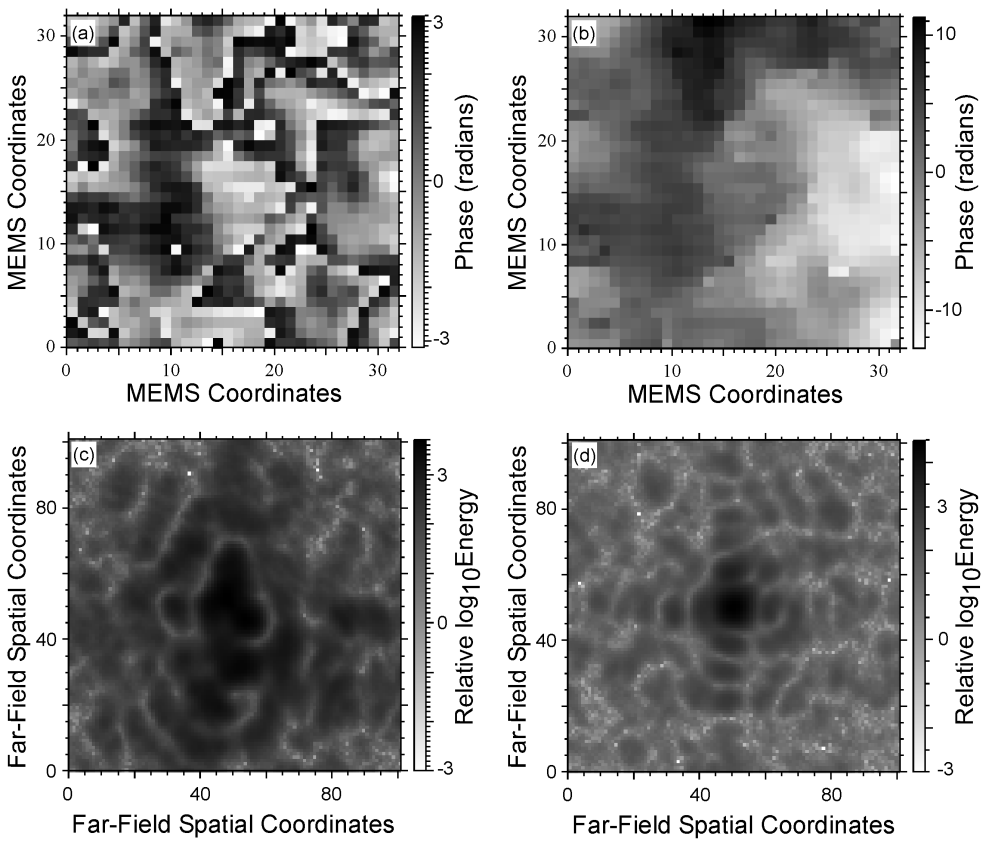

Fig. 7. Measurements examining the effects of Kolmogorov phase screen errors across the aperture. The wrapped and unwrapped phases are displayed in Fig. 7a and 7b, respectively. The far-field intensity patterns for the uncorrected and corrected far-field intensity measurements are shown in Fig. 7c and Fig. 7d, respectively.

The measured unwrapped phase profile in Fig. 7b can be analysed to determine the structure function, $D\phi(r)$, of the phase aberration. A Von Karman spectrum was fit to the structure function as shown in Fig. 8. Simulations of the ARC beam line have indicated that the Strehl ratio will be close to a value of, S_r ~0.09.[19] This result was obtained via simulations of the ARC beamline using the PROP92 beam propagation code.[20] The Von Karman turbulence profile fit to the structure function calculated from the measured phase profile in Fig. 7b consisted of a Fried parameter equal to r_o=D/18 and the outer scale length equal to L_o=1.8D. This is consistent with the values expected on the ARC beam line and produce Strehl ratios close to the values expected from the ARC simulations. The Strehl ratio from the applied phase plate, as determined by analyzing Fig. 7c, was S_r =0.087.

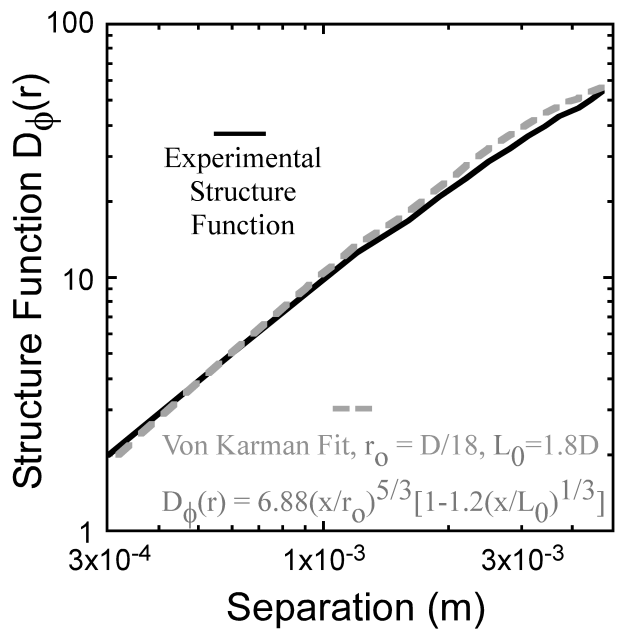

Fig. 8. Structure function for the unwrapped phase profile corresponding to the applied phase plate. The solid black line represents the measured structure function and the dashed grey line is the analytical Von Karman structure function with the Fried parameter equal to r_o=D/18 and the outer scale length equal to L_0=1.8D.

Interferometric characterization of the pixilated MEMS deformable mirror indicated that the maximum corrected Strehl ratio of the entire 32x32 device, due to the surface profile of the MEMS device itself, is S_r = 0.88 at 1.053 μm.[6] This is due almost entirely to sharp gradients near the edges of the device arising from the polishing procedure used on the current MEMS device. The MEMS manufacturer has several methods to significantly reduce the phase gradients nears the edges of the MEMS mirrors and this will significantly reduce the reduction in Strehl ratio in future devices. On the current device, the reduction in Strehl ratio can be significantly reduced by using the inner 26x26 pixels.

4. PISTON-REMOVED PHASE VARIANCE

The piston-removed phase variance represents both the phase variance of the aberrated wave-front incident on a telescope with no adaptive optics system present and also the wave-front fitting error expected from an adaptive optics system with piston-only correction. These errors represent the reduction in the Strehl ratio resulting from the inability of a finite sized aperture to fully correct the turbulence spectrum with spatial wavelengths less than or on the order of the size of the aperture or sub-aperture in the case of the wave-front fitting error. For the piston-only MEMS device used for this article the fitting error is equivalent to the piston-removed phase variance. The intensity distribution in the focal plane is found by Fourier transforming the product of the phase screen and aperture or sub-aperture transfer functions. The Strehl ratio only requires the ratio of the intensity with the atmospheric transfer function and without along the optical axis. The atmospheric optical transfer function is related to the phase structure function, $D_\varphi(\rho)$, through the relation $OTF(\rho)=\exp\{-0.5*D_\varphi(\rho)\}$.[7] The phase structure function is calculated from an integral involving the spatial power spectrum of the turbulence expressed above. In particular, the phase structure function, $D_\varphi(\rho)$, can be calculated from the spatial power spectrum using the equation[21,22,23]

$$D_\varphi(\rho) = 4\pi \int_0^\infty \kappa d\kappa \left[1 - J_0(\kappa\rho)\right] F_\varphi(\kappa), \qquad (3$$

where $F_\varphi(\kappa)_{VK} = 2\pi k^2 L \Phi_n(\kappa)$, $\Phi_n(\kappa)$ is the three-dimensional Von Karman spectrum of refractive index fluctuations, L is the propagation length and k is the wavenumber of the probe beam. $\Phi_n(\kappa)$ is defined by $\Phi_n(\kappa) = 0.033 C_N^2(\kappa^2+\kappa_o^2)^{-11/6}$, where C_n^2 is the index of refraction constant and $\kappa_o = 2\pi/L_o$. Upon performing the integration, the phase structure function can be expressed as

$$D_{\varphi}(\rho)=3.696(r_o\kappa_o)^{-5/3}\left[1-\frac{5(\rho\kappa_o)^{5/6}}{3(2)^{5/6}\Gamma(11/6)}K_{5/6}(\rho\kappa_o)\right]. \quad (4$$

Assuming that $(\rho\kappa_o)<<1$ and expanding the first three most significant terms of the Bessel function, $D_\varphi(\rho)$ can be reduced to $D_\varphi(\rho)\sim 6.88(\rho/r_o)^{5/3}(1-0.8(\rho\kappa_o)^{1/3})$.[23] In the limit that $\kappa_o(L_o)$ approaches zero(∞), this reduces to the phase structure function calculated using a Kolmogorov turbulence spectrum.

The piston-removed phase variance, and also the wave-front fitting error associated with a piston-only correction, for a square sub-aperture, can then be approximated as the integral of the product of the optical transfer function of the atmosphere and the input telescope, assuming a square aperture. This is expressed as

$$\sigma^2 \approx \frac{1}{2d^2}\int_{-d}^{d}\int_{-d}^{d} dxdy\left(1-\left|\frac{x}{d}\right|\right)\left(1-\left|\frac{y}{d}\right|\right)D_\varphi(x,y), \quad (5$$

where d is the length of one side of the square aperture for the piston-removed phase variance and the sub-aperture in the case of the wave-front fitting error. By converting to cylindrical coordinates, $x = r\cos(\theta)$ and $y = r\sin(\theta)$ and integrating over one octant of the aperture, the piston-removed phase variance for a square aperture can be expressed as

$$\sigma^2 \approx \frac{4}{d^2}\int_0^{\pi/4}\int_0^{d/\cos(\theta)} rdrd\theta\left(1-\frac{r\cos(\theta)}{d}\right)\left(1-\frac{r\sin(\theta)}{d}\right)D_\varphi(r), \quad (6$$

where d is the length of one side of the square aperture. This integral may be evaluated by expanding the modified Bessel function of the second kind, contained in the structure function, into a power series representation and performing the integration. The resulting power series solution for Eq. 6 can be written as

$$\begin{aligned}\sigma^2 &= 1.31\left(\frac{d}{r_o}\right)^{5/3}\left\{1-0.682(d\kappa_o)^{1/3}+0.073(d\kappa_o)^2\right\}\\ &-46.18\left(\frac{d}{r_o}\right)^{5/3}\sum_{m=2}^{\infty}\frac{(d\kappa_o)^{2m-5/3}}{\Gamma(m+1/6)m!2^{2m-5/6}(2m+3)(2m+2)}x\\ &\left\{\frac{\left[1-2^{m+1}\right]}{2m+4}+\int_0^{\pi/4}\frac{d\theta}{(\cos\theta)^{m+2}}\right\} \quad (7\\ &+46.18\left(\frac{d}{r_o}\right)^{5/3}\sum_{m=2}^{\infty}\frac{(d\kappa_o)^{2m}}{\Gamma(m+11/6)m!2^{2m+5/6}(2m+14/3)(2m+11/3)}x\\ &\left\{\frac{\left[1-2^{m+11/6}\right]}{2m+17/3}+\int_0^{\pi/4}\frac{d\theta}{(\cos\theta)^{2m+11/3}}\right\}\end{aligned}$$

In the limit that $\kappa_o = 0$, this expression reduces to the result previously obtained for the piston-removed phase variance with a Kolmogorov turbulence spectrum, which also corresponds to the fitting error obtained with a piston-only MEMS device with square actuators.[7]

The phase plate was measured and determined to contain a Fried parameter equal to $r_o=D/18$ and an outer scale length equal to $L_o=1.8D$, where $\kappa_o = 2\pi/L_o$. The phase variance should be approximately $\sigma^2=1.31(d/r_o)^{5/3}(1-0.68(d\kappa_o)^{1/3})$ or $\sigma^2=0.34$ rad^2. The maximum Strehl ratio achievable with this phase plate, using a piston only MEMS device, is then $S_r = 0.71$ which agrees well with the measured Strehl ratio of $S_r = 0.66$.

5. STREHL RATIO IMPROVEMENTS

A couple of problems with the wave-front sensor camera were identified that lead to a reduction in the achievable Strehl ratio. One of these problems is that the charge is not zeroed out after the camera is read out. To quantify this behaviour the laser was triggered once and the camera was read out fifty times. The results of this study are shown below in Fig. 9a. For this acquisition run the laser was triggered before the second camera read and should have been fully read out on camera read number 2. A negative residual charge, relative to the camera background, of approximately 12 digital numbers was measured on camera read 3 for an applied reference signal before the second read of approximately 1200 digital numbers. On the fourth read the signal swings positive by approximately 2 counts and slowly decays to zero over the next 10 camera reads. This effect can be ameliorated by either incorporating this behaviour into the measurement, which requires accessing previous wave-front camera acquisitions to correctly determine the intensity due to the current acquisition, or by firing the laser once for every n number of camera reads and discarding the n-1 camera acquisitions which are simply used to remove all residual charge from the camera. This effect primarily influences the temporal behaviour of the system by retaining a partial signal that is due to previous measurements. A second peculiarity discovered was an inconsistency in the background subtraction which could be related to the persistence issue stated above. In this case the reference laser was triggered along with the camera and the camera was read out for 400 reads. A reference intensity was taken from a sub-region in the image for both the sine and cosine channels and used to scale an average reference image and subtract the scaled image from the current measurement. The results of these differences averaged over the respective channels should produce slight variations around zero counts with the sine and cosine channels correlated with one another. The results of this test are shown below in Fig. 9b. Although the sine and cosine channels are correlated over a small fraction of the acquisitions, there are a substantial number where the sine and cosine channels differ by as many as four digital numbers which limits the precision that the reference intensity can be subtracted from the interferogram and as a consequence in the overall achievable Strehl ratio. Numerical simulations have indicated that an error of 0.3% in the reference beam subtraction, 4 counts out of the roughly 1200 counts, will reduce the Strehl ratio by ~0.03.[6,12]

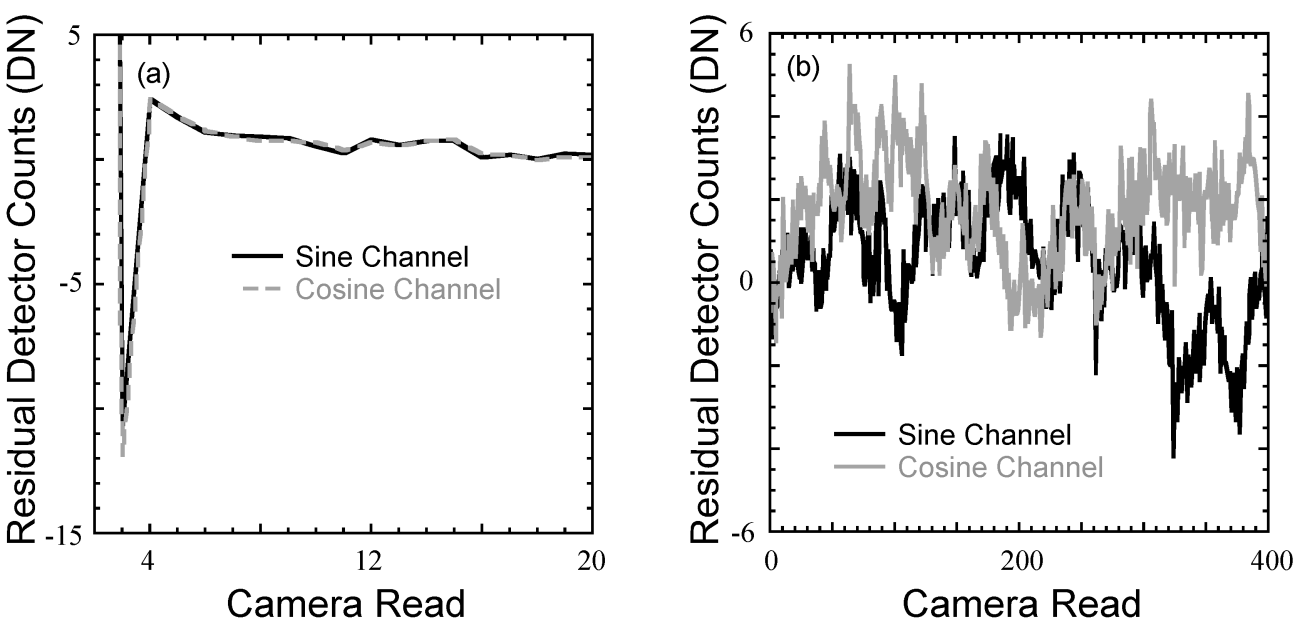

Fig. 9. Background subtraction and residual charge data from the Sensors Unlimited wave-front sensor camera. Fig. 9a represents the residual charge on the wave-front sensor camera as a function of camera reads. The laser was applied to the focal plane array before the second camera read. Fig. 9b represents the residual charge on the wave-front sensor camera after the average intensity has been subtracted.

6. SUMMARY

In this article results were presented on a testbed used to evaluate the performance of an interferometric adaptive optics system. These measurements included quantification of the reduction in Strehl ratio incurred when using the MEMS device to correct for pointing errors in the system. Analytic calculations were performed to evaluate the reductions in Strehl ratio as a function of waves of tip/tilt applied across the MEMS device and shown to be in excellent agreement with the measured data when the analytic expression was adjusted for residual aberrations in the optical system. The interferometric adaptive optics system was shown to correct for a piston, tip/tilt error between adjacent rectangular apertures, the geometry expected for the National ignition Facility. In this case a Strehl ratio of 0.76 was achieved. The interferometric adaptive optics system was also used to correct for a phase plate aberration of similar magnitude as expected from simulations on the ARC beam line. The interferometric adaptive optics system achieved a Strehl ratio of 0.66 which is very close to the theoretical Strehl ratio of 0.71. Several factors causing reductions in the achievable Strehl ratio were identified and will be eliminated or reduced before implementing the system on the National Ignition facility.

ACKNOWLEDGEMENTS

The authors would like to than Everett Utterback and Steve Jones for assistance in programming the data acquisition system for the testbed. This work was performed under the auspices of the U.S. Department of Energy by Lawrence Livermore National Laboratory under Contract DE-AC52-07NA27344.

REFERENCES

[1] R. A. Zacharias, N. R. Beer, E.S. Bliss, S. C. Burkhart, S. J. Cohen, S. B. Sutton, R. L. Van Atta, S. E. Winters, J. T. Salmon, M. R. Latta, C. J. Stolz, D. C. Pigg, and T. J. Arnold, Alignment and wavefront control systems of the National Ignition Facility Opt. Eng. **43** (12), 2873 (2004).

[2] D.M. Pennington, C.G. Brown, T.E. Cowan, S.P. Hatchett, E. Henry, S. Herman, M. Kartz, M. Key, J. Koch, A.J. Mackinnon, M.D. Perry, T.W. Phillips, M. Roth, T.C. Sangster, M. Singh, R.A. Snavely, M. Stoyer, B.C. Stuart, and S.C. Wilks, Report No. UCRL-JC-140019, 2000.

[3] Robert Hartley, Michael Kartz, William Behrenclt, Andy Hines, George Pollock, Erlan Bliss, Thad Salmon, Scott Winters, Bruno Van Wonterghem, and Richard Zacharias, Wavefront correction for static and dynamic aberrations to within 1 second of the system shot in the NIF Beamlet demonstration facility SPIE **3047**, 294 (1997).

[4] Ji-Ping Zou, Anne-Marie Sautivet, Jérôme Fils, Luc Martin, Kahina Abdeli, Christian Sauteret, and Benoit Wattellier, Optimization of the dynamic wavefront control of a pulsed kilojoule/nanosecond-petawatt laser facility Applied Optics **47** (5), 704 (2008).

[5] C.N. Danson, P.A. Brummitt, R.J. Clarke, J.L. Collier, B. Fell, A.J. Frackiewicz, S. Hancock, S. Hawkes, C. Hernandez-Gomez, P. Holligan, M.H.R. Hutchinson, A. Kidd, W.J. Lester, I.O. Musgrave, D. Neely, D.R. Neville, P.A. Norreys, D.A. Pepler, C.J. Reason, W. Shaikh, T.B.Winstone, R.W.W. Wyatt, and B.E.Wyborn, Vulcan Petawatt—an ultra-high-intensity interaction facility Nucl. Fusion **44**, 239 (2004).

[6] Kevin L. Baker, Eddy A. Stappaerts, Doug C. Homoelle, Mark A. Henessian, Erlan S. Bliss, Craig W. Siders, and Chris P.J. Barty, Interferometric adaptive optics for high-power laser pointing and wavefront control and phasing J. Micro/Nanolith.MEMS MOEMS **8** (3), 033040 (2009).

[7] John W. Hardy, *Adaptive Optics for Astronomical Telescopes*. (Oxford University Press, Oxford, 1998).

[8] K.L. Baker, E.A. Stappaerts, D. Gavel, S.C. Wilks, J. Tucker, D.A. Silva, J. Olsen, S.S. Olivier, P.E. Young, M.W. Kartz, L.M. Flath, P. Kruelevitch, J. Crawford, and O. Azucena, High-speed horizontal-path atmospheric turbulence correction using a large actuator-number MEMS spatial light modulator in an interferometric phase conjugation engine Opt. Lett. **29** (15), 1731 (2004).

[9] James Notaras and Carl Paterson, Point-diffrction interferometer for atmospheric daptive optics in strong scintillation Optics Communications **281**, 360 (2008).

[10] Gordon D. Love, Thomas J. D. Oag, and Andrew K. Kirby, Common path interferometric wavefront sensor for extreme adaptive optics Optics Express **13** (9), 3491 (2005).

[11] K.L. Baker, Interferometric Wavefront Sensors for High Contrast Imaging Optics Express **14**, 10970 (2006).

[12] K.L. Baker, E.A. Stappaerts, D.C. Homoelle, M.A. Hennesian, E.S. Bliss, E. Utterback, C.W. Siders, and C.P.J. Barty, Interferometric adaptive optics for high power laser pointing, wave-front control and phasing SPIE **7209**, 720907 (2009).

[13] K.L. Baker, E.A. Stappaerts, S.C. Wilks, D. Gavel, P.E. Young, J. Tucker, D.A. Silva, S.S. Olivier, and J. Olsen, Performance of a phase-conjugate-engine implementing a finite-bit phase correction Opt. Lett. **29** (5), 980 (2004).

[14] Gordon D. Love, Nigel Andrews, Philip Burch, David Buscher, Peter Doel, Colin Dunlop, John Major, Richard Myers, Alan Purvis, Ray Sharples, Andrew Vick, Andrew Zadrozny, Sergio R. Restaino, and Andreas Glindemann, Binary adaptive optics: atmospheric wave-front correction with a half-wave phase shifter Applied Optics **34** (27), 6058 (1995).

[15] D. Homoelle, K.L. Baker, E. Utterback, C.W. Siders, and C.P.J. Barty, presented at the Ultrafast Optics, France, 2009.

[16] R.M. Goldstein, H.A. Zebker, and C.L. Werner, Satellite radar interferometry: two-dimensional phase unwrapping Radio Science **23** (4), 713 (1988).

[17] [1]Dennis C. Ghiglia and Mark D. Pritt, *Two-Dimensional Phase Unwrapping*. (John Wiley & Sons, Inc., New York, 1998).

[18] K.L. Baker and D.A. Silva, Evaluation of Two-Dimensional Phase Unwrapping Algorithms for Interferometric Characterization of Liquid-Crystal Spatial Light Modulators The Open Optics Journal **2**, 48 (2008).

[19] M.A. Henessian.

[20] R.A. Sacks, M.A. Henesian, S.W. Haney, and J.B. Trenholme, Report No. UCRL-LR-105821-96, 1996.

[21] George C. Valley, Long- and short-term Strehl ratios for turbulence with finite inner and outer scales Applied Optics **18** (7), 984 (1979).

[22] Patrick M. Harrington and Byron M. Welsh, Frequency-domain analysis of an adaptive optical system's temporal response Optical Engineering **33** (7), 2336 (1994).

[23] R.F. Lutomirski and H.T. Yura, Wave Structure Function and Mutual Coherence Function of an Optical Wave in a Turbulent Atmosphere Journal of the Optical Society of America, **61** (4), 482 (1971).